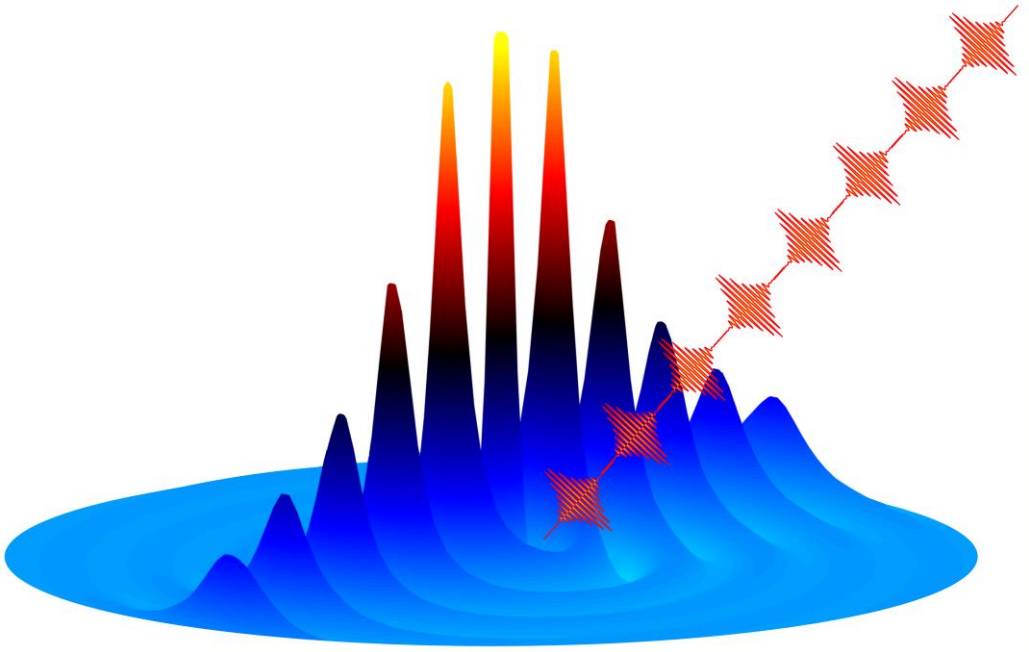

Excitation and Detection of Spinwaves with Light

BACHELOR THESIS PROJECT WITH A MAJOR IN PHYSICS
2020, 180 HEC
First Cycle

Hannes Bergström
Ossian Lundgren
Isac Rydbjer
Mathias Samuelsson
Mathias Örtenberg Toftås
Nils Tornberg

DEPARTMENT OF PHYSICS

CHALMERS UNIVERSITY OF TECHNOLOGY
UNIVERSITY OF GOTHENBURG
Gothenburg, Sweden 2020

Excitation and Detection of Spinwaves with Light

BACHELOR THESIS PROJECT WITH A MAJOR IN PHYSICS

H. Bergström O. Lundgren I. Rydbjer
M. Samuelsson M. Toftås N. Tornberg

Supervisor: Ahmad A. Awad
June 24, 2020
Gothenburg

GÖTEBORGS
UNIVERSITET

CHALMERS

Abstract

Spinwaves (SWs) are a collective excitation of the local spin moments in a magnetic ordered medium. Spinwaves can be excited electrically using microwave sources, direct currents, and by focused optical short pulses on a thin magnetic film. Spinwaves are utilized in many emerging concepts for new technologies. But the SWs in almost all proof-of-principle SW devices are generated using electrical currents, inductive transducers and antenna structures, which severely limit scalability and the operating frequencies. It has recently been shown that it is possible to create and control SWs of high amplitude using a high repetition rate femtosecond pulsed laser (fs-laser). However, the impact of different material parameters is still unknown as the original demonstration of the technique was conducted using a single NiFe (Py) ferromagnetic thin film with a thickness (20 nm) comparable to the laser penetration depth.

In this project, we investigate SWs excited by fs-laser pulse trains (laser comb with 1 GHz repetition rate) using Brillouin Light Scattering (BLS) microscopy. We demonstrate that previous results are reproducible using a much thicker 100 nm film. Furthermore, in such thicker films, optical stimulation of SWs is clearly observed to be efficient with harmonic frequencies up to 15 multiples of the repetition rate of the pulsed fs-laser. The SW BLS intensity exhibits a stronger than parabolic dependence on the laser fluence, and the heat-induced demagnetization is found to follow the Bloch $T^{3/2}$ law.

Moreover, we show that the optical excitation of sustained SWs is reproducible over a wide range of film thicknesses (20-100 nm) and the efficiency is inversely proportional to the film thickness. In order to further corroborate our conclusions and to enhance the spin wave excitation efficiency, additional measurements on a gold-doped Py sample were done. They showed the expected enhanced excitation efficiency compared to the pristine film.

Acknowledgements

The group would first and foremost like to express its gratitude towards our supervisor Ahmad Awad, who not only gave us the opportunity to work on this project, but also offered his continuous support with experiments, interpretation of data and writing. Furthermore, his lectures and expertise in the field helped greatly with unraveling a subject previously unfamiliar to all of us. We would also like to thank Shreyas Muralidhar for assisting us with experiments and sample fabrication. One can only imagine how many more hours we would have spent trying to get the setup to work if he hadn't been there to fix it. An additional thank you goes out to Martina Ahlberg and Roman Khymyn. Martina for reviewing the thesis and giving us constructive feedback and Roman for his help with theoretical derivations. Finally, we would like to thank the Department of Physics at the University of Gothenburg, and more specifically the Applied Spintronics Group for their help in this project, allowing us to occupy their facilities and utilize their valuable experimental setup and resources, giving us hands on experience with scientific research.

Acronyms

BLS Brillouin Light Scattering. 6, 10–13, 16–21, 24, 26, 27

FMR Ferromagnetic Resonance. 3, 15, 17, 18, 26

MSBC Magneto-Static Boundary Conditions. 4, 5

PSSW Perpendicular Standing Spinwave. 5, 6, 17, 18, 20–22, 24–26

SW Spinwave. 1–3, 5, 7–12, 16–27

Glossary

Bloch law A first order approximation of the temperature dependence of a materials spontaneous magnetization. 9

saturation magnetization A measurement of a materials highest possible magnetization. 3

Contents

1 Introduction

In 1930 Felix Bloch published a short paper on the interactions between metallic electrons and a concept he called spinwaves [1, 2]. The idea, that Bloch had while visiting the Physical Laboratory of the Rijks University, involved electron spins flipping and interacting with each other and it was used to explain the reduction of the magnetization as a function of temperature. The theory not only furthered our understanding of magnetic materials, but is also essential in the emerging field of magnonics [3, 4, 5].

Spinwaves (SWs) can be described as collective perturbations of the magnetic order (magnetization) of a magnetic material. Magnetization can be seen as the collective behavior of many ordered spin states, i.e. the magnetic moment. When a strong external magnetic field is applied to a ferromagnetic solid, the magnetic moments will align along its direction. This alignment, or any other dynamics the magnetic moment experiences, is performed through a damped precessional motion [6]. The collective precession of these moments is the SW. Spinwaves are quantized and consist of quasiparticles called magnons, analogous to the phonons of the atomic vibrational waves in a solid [7, 8].

Spinwaves have high potential for applications in signal generation and future alternative electronics, known as magnon spintronics and magnonics, where the SWs replace electrons as information carriers [9, 3, 10]. Devices based on SWs operate at a high frequency (GHz to THz) relevant for fast communications and processing, due to the intrinsic high-frequency nature of SWs. This has potential for implementation in wave-based computing and other alternative computing schemes such as neuromorphic computing [11, 12]. Another attractive feature of SWs is that they can be utilized without application of electrical charge currents, which are the leading power drain in electronics, through significant Joule heating dissipation. Furthermore, magnons are several orders of magnitudes smaller than their electrical signal counterparts operating at the same frequency, which directly offers more compact spintronic and magnonic components, compared to electrical ones [7, 13].

Despite the concept being very promising, there are several obstacles that one must overcome in order to construct adequate magnonic devices. One of the major bottlenecks is the local generation and channeling of the SWs. There are several ways of exciting spinwaves, such as through microwave currents, short magnetic pulses [8], and DC currents [14]. Although these are well-established forms of SW generation, they are currently not meeting the demand for high frequency, efficiency and controllability beyond the commercially available electronics. Moreover, these methods often require nanostructuring to function, which complicates the device design and fabrication. Being able to selectively generate and manipulate spinwaves is a necessity to construct magnonic devices. In this project, we will therefore, examine a relatively new method of SW generation, namely excitation through laser pulses [15].

Spinwaves can be excited via laser light through a process known as ultrafast demagnetization, described in more detail in section 2.6. This contactless approach has several benefits such as simpler device construction. That said, the method is also associated with its own set of obstacles. In particular, the SWs generated this way are quickly dampened and they can therefore be difficult to detect. However, recent studies have shown that it is possible to maintain an efficient generation of SWs at high frequencies using a pulsed laser with a high repetition rate [13, 16, 17]. This new approach of generating SWs without electrical means has a tremendous potential to advance both magnonic research and devices, resolving frequency and design constraints. Such a laser configuration is utilized in the unique experimental setup used in this project and the optical method of SW excitation via laser is evaluated.

Furthermore, studies previously referred to have been limited to investigations of a single sample type. To fully utilize this new method, the behavior of the SWs must be characterized for materials of different dimensions and properties. Thus, in this project, we aim to further the scientific understanding of this method by studying the properties of thermally and optically excited SWs as a function of the pulsed laser power, the thickness of the sample film, and the strength of the applied magnetic field. Spinwaves will be examined in a nickel-iron alloy (Py) and their properties will be compared with those of doped Py films in order to study the effects of the Curie temperature.

2 Spinwaves

2.1 Precession of Magnetic Moments

A typical ferromagnetic material consists of a single or multiple magnetic domains, that are clusters with uniform magnetization. Inside each magnetic domain, the magnetization can be represented by a set of magnetization vectors all pointing in the same direction [6]. The field strength needed to align all domains is called the saturation field. In addition to its static properties, the magnetization also exhibit dynamics in the form of a damped precessional motion. If an external magnetic field is applied, these magnetic moments will tend to align with the field like a compass needle. The magnetization dynamics can be described by a phenomenological equation called the Landau-Lifshitz-Gilbert equation [18]

$$\frac{d\vec{M}}{dt} = -\gamma(\vec{M} \times \vec{H}_{\text{eff}}) + \frac{G}{\gamma M^2}(\vec{M} \times \frac{\partial \vec{M}}{\partial t}), \tag{1}$$

where the first term on the right-hand side corresponds to the precessional motion and the second to the magnetic damping. In the equation, γ is the gyromagnetic ratio, G is the Gilbert damping constant, $\vec{M}$ is the magnetization moment, and $\vec{H}_{\text{eff}}$ the effective magnetic field. By solving the precessional part of this equation of motion, which is done by ignoring the damping component, one obtains the Kittel equation [6]. Assuming a thin film and that the applied magnetic field is in the film plane, the Kittel equation is reduced to the following form [6]

$$f_{\text{r}} = \frac{\gamma}{2\pi}\mu_0\sqrt{(H_{\text{ext}} + H_{\text{k}})(H_{\text{ext}} + M_{\text{s}})}. \tag{2}$$

Where M_{s} is the saturation magnetization, H_{ext} the strength of the applied magnetic field, μ_0 is the permeability of vacuum and H_{k} is the in-plane magnetic anisotropy. The magnetic anisotropy is a parameter that defines a preferred direction for the alignment of the magnetization [18]. f_{r} is the frequency of the precessing magnetic moments and it is called the ferromagnetic resonance (FMR) frequency.

While the FMR describes the in-phase precession of all the magnetic moments, higher modes of motion exist where the magnetic moments have a constant phase offset from their neighbors, thus forming a wave. This is seen in Fig. 1 and these waves are higher mode SWs.

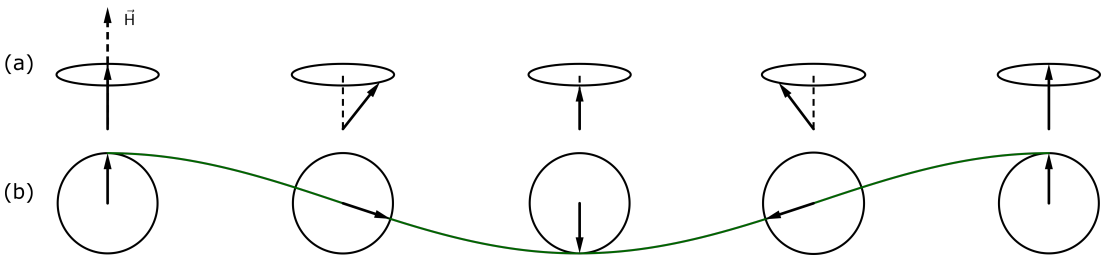

Figure 1: Spinwave illustration, (a) side view of the magnetic moments, (b) top view of the same magnetic moments. The green line shows the spinwave profile.

As the magnetic moments precess, the component of the moments pointing along their original direction decreases. The more energy that is added to the system, the more these magnetic moments deviate from their original directions. When no component is left in the original direction, the net magnetic moment is zero. The Curie temperature defines the thermal energy needed for this complete loss of ferromagnetic order. This is a simplified view of how the temperature affects the magnetization.

2.2 External and Internal Field

The magnetic field inside the film will not be the same as the externally applied field. The spinwave dispersion and the behavior of the magnetization are both dependent on the magnitude and the direction of the internal magnetic field. Thus we need to solve the magneto-static boundary conditions (MSBC) for the film to determine the internal field. Using the Cartesian coordinate system in Fig. 2, the MSBC have the following form [19]:

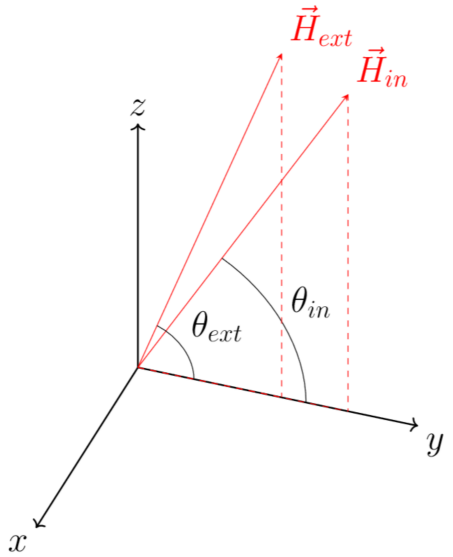

$$\begin{cases} H_{\text{in}}\cos(\theta_{\text{in}}) = H_{\text{ext}}\cos(\theta_{\text{ext}}) - M_{\text{s}}\cos(\theta_{\text{in}}) \\ M_{\text{s}}\sin(2\theta_{\text{in}}) = 2H_{\text{ext}}\sin(\theta_{\text{in}} - \theta_{\text{ext}}). \end{cases} \tag{3}$$

Figure 2: Magnetic field coordinates, coordinate system showing the applied external field and the internal field in a magnetic film with governing boundary conditions.

Where H_{ext} and H_{in} in Eq. (3) are the external and internal field, respectively, and θ_{ext} and θ_{in} are the external and internal angle from the surface plane of the film. The external angle and field in relation to the sample can be seen in Fig. 9. Due to these conditions, the Kittel equation (2) takes the following form in ferromagnetic films [18]:

$$f_r = \frac{\gamma}{2\pi}\mu_0\sqrt{(H_{in}+H_k)(H_{in}+M_s\cos^2(\theta_{in}))}. \tag{4}$$

The internal field and angle is important for describing the frequency dependence and the dispersion of the higher SW modes, especially as our setup has the field applied at oblique angles. This can be seen in Eq. (5) in the following section.

2.3 General Spinwave Modes and Dispersion

Spinwaves created by phase-offset precession of the magnetic moment have a finite wavelength, in contrast to the in-phase FMR precession. The frequency of the higher mode SWs is described by a dispersion relation. The dispersion of the SWs can be obtained using a simplified version of Eq. (45) from [19] which reads as follows:

$$f = \frac{\gamma\mu_0}{2\pi}\sqrt{(H_{in}+l_{ex}^2M_sk^2)(H_{in}+l_{ex}^2M_sk^2+M_sF_0)}, \tag{5}$$

where $l_{ex} = \sqrt{2A_{ex}/\mu_0M_s^2}$, H_{in} and θ_{in} are the magnitude and the out-of-plane angle of the internal field, respectively. These are calculated by solving the MSBC for the film as seen in Eq. (3). A_{ex} is the exchange stiffness and F_0 in Eq. (5) is given by Eq. (46) from [19], defining the SW wave vector dependence on sample thickness and propagation direction. k is the absolute value of the wavevector $\vec{k}$ in all of the equations above. Using this, calculations of dipole-exchange SWs and magnetostatic waves in the ferromagnetic samples can be made [19]. Eq. (5) allows us to calculate the characteristics of spinwaves in ferromagnetic thin films. Furthermore, we can use the measured SW frequency versus field to extract the magnetic properties M_s, A_{ex} and γ of the sample.

2.4 Perpendicular Standing Spinwaves

The dispersion relation described in Eq. (5), when applied for the direction along the thickness of a thin film, gives rise to quantized standing waves perpendicular to the surface of the film, so called perpendicular standing spinwaves (PSSWs). These waves have a quantized nature as the thinness of the film forces the k-vectors apart. This can be understood by analogy to classical electromagnetic waves in a resonant cavity. As the size of the cavity increases the differences in frequency, and thus also energy, between different wave modes decrease. This behaviour will also be seen for PSSWs as the thickness of the film increases. The difference in frequency is given by a modified

version of Eq. (5) that takes the following form:

$$f_{\mathrm{PSSW}} = \frac{\gamma}{2\pi}\mu_0\sqrt{(H_{\mathrm{in}} + l_{\mathrm{ex}}^2 M_{\mathrm{s}} k^2)(H_{\mathrm{in}} + l_{\mathrm{ex}}^2 M_{\mathrm{s}} k^2 + M_{\mathrm{s}}\cos^2(\theta_{\mathrm{in}}))}. \tag{6}$$

Different modes of PSSWs are illustrated in Fig. 3, where $k = \pi n/L$, n is an integer, L is the thickness of the sample film and the wave vector $\vec{k}$ here is out-of-plane wave vector.

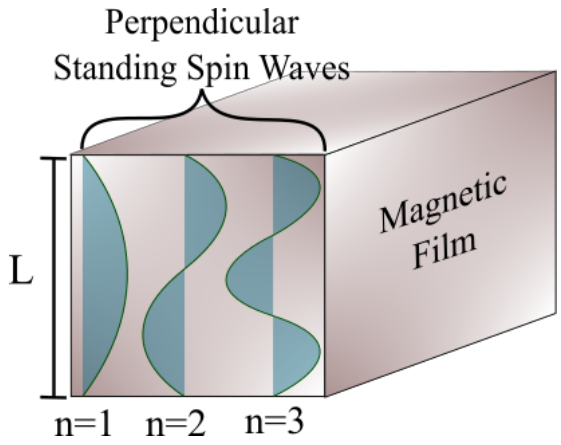

Figure 3: PSSW illustration. Profile of different PSSWs modes in a magnetic film of thickness L.

2.5 Brillouin Light Scattering

When a photon collides with a magnon, it will scatter inelastically. The photon will either gain energy or lose energy, the interaction being that the photon either absorbs or creates a magnon. These processes are known as Stokes and Anti-Stokes respectively. The described inelastic scattering process as a whole is known as Brillouin light scattering (BLS), and the process is applicable to other quasiparticles with the same frequency range, e.g. acoustic phonons, see Fig. 4. In the quantum framework, the magnons share the same energy level as photons with the same frequency. Thus the energy and frequency change of the scattered photon corresponds to the absorbed or created magnon. We summarize this in Eqs. (7a) and (7b) [7].

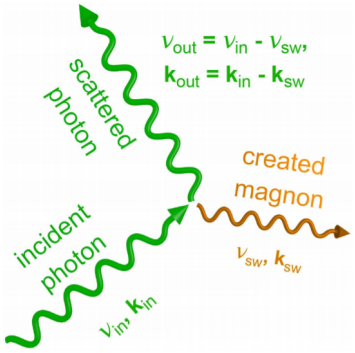

$$h\nu_{\text{pho}}^{\text{out}} = h\nu_{\text{pho}}^{\text{in}} \pm h\nu_{\text{mag}} \tag{7a}$$
$$\hbar\mathbf{k}_{\text{pho}}^{\text{out}} = \hbar\mathbf{k}_{\text{pho}}^{\text{in}} \pm \hbar\mathbf{k}_{\text{mag}} \tag{7b}$$

Figure 4: Brillouin light scattering. The generation of a magnon (Stokes process) is shown along with the governing energy and momentum conservation equations of both the generation and annihilation processes. Figure by T. Sebastian et al. [7], licensed under CC BY 4.0.

Furthermore, the polarization of the scattered photon is rotated by 90° with respect to its initial polarization when it scatters with a magnon. This change in polarization makes it possible to differentiate photons scattered off of magnons from unwanted reflected photons as well as photons scattered from phonons, as they do not suffer polarization change. [7]

2.6 Ultrafast Demagnetization

The manipulation of magnetic order by ultrashort laser pulses was reported back in 1997 [20]. When a femtosecond (fs) laser is fired on a magnetically ordered thin film, the laser pulses rapidly increase the local temperature and fast sub-picosecond demagnetization occurs. The manipulation mechanisms arise from the interaction of photons with electrons, spins, and the lattice, and angular momentum transfer between them. A simple model that describes this local behavior is the three-temperature model [21, 22]. An illustration of the model can be seen in Fig. 5. The electrons that primarily absorb the energy of the photons interact with the lattice and the spin system in the material, resulting in the demagnetization of the material. The temperature then equilibrates on a much larger time scale, while the magnetization recovers within picoseconds. This local perturbation of the magnetization, both the demagnetization and remagnetization, generates SWs in the material [15].

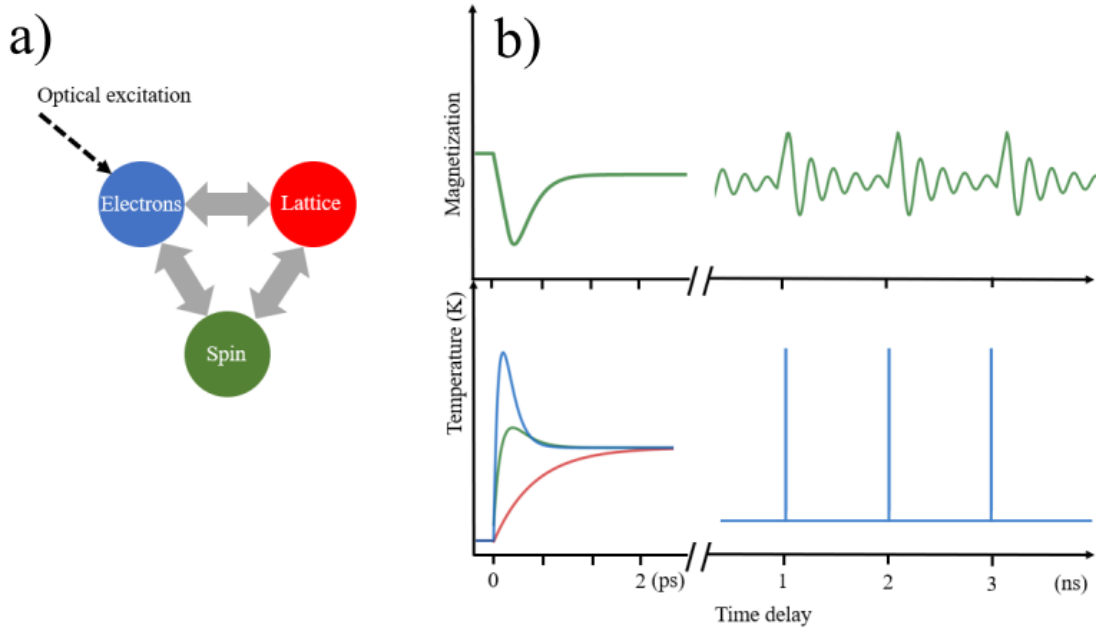

Figure 5: Ultrafast laser induced demagnetization and SW triggering. Illustration of the excitation mechanism. (a) Schematic view of the phenomenological three-temperature model, that describes the energy transfer from the optically excited hot electrons to both the spin and lattice sub-systems and subsequently the energy equilibration between those subsystems. (b) The three temperature model timescales and the corresponding ultrafast demagnetization and magnetization on a picosecond time scale and the resulting SW excitation sustaining on a nanosecond timescale.

Since the spinwaves have a decay time on the order of nanoseconds, it is not possible to study the SW dynamics directly with averaging technology. Therefore pump-probe techniques are primarily used for the characterization of this phenomena [22]. However, by continuously exciting SWs with laser pulses at a very high frequency, the SW dynamics are not allowed to be damped out. This makes it possible to continously create sustainable SWs by optical means, either by the inverse Faraday effect in insulating ferrimagnets [16, 17] or more recently, demagnetization [13].

The intensity of the SWs is a function of demagnetization. However, the demagnetization occurs around a fixed point along the magnetization curve of the material. Depending on where along this curve the material is, the same laser pulse can achieve different amounts of demagnetization. Thus, the SW intensity is also a function of temperature. A schematic representation of this dependence on the temperature can be seen in Fig. 6.

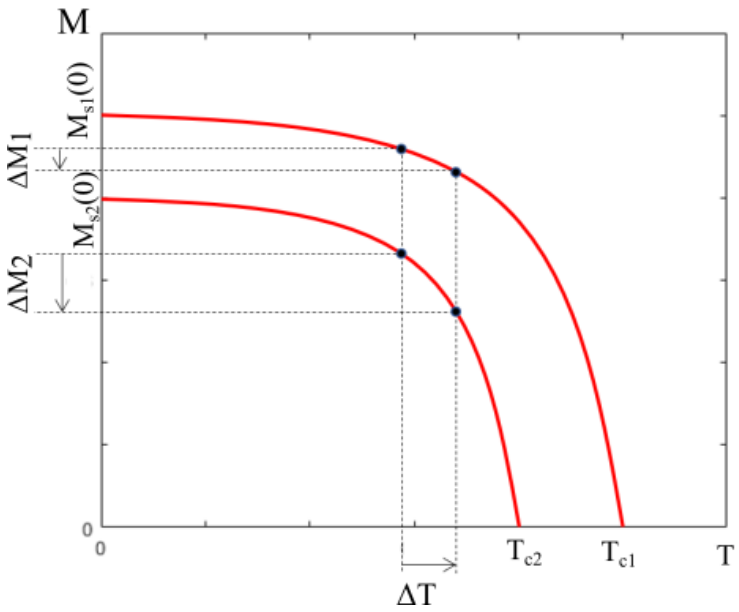

Figure 6: Magnetization dependence on temperature. The magnetization for two materials as a function of temperature. Note how a temperature change of ΔT results in different magnetizations changes ΔM for the two materials.

The curves in Fig. 6 present the magnetization of two ferromagnetic materials with different Curie temperatures. Above the Curie temperature, the magnetization of the material will be zero. At low temperatures, the magnetization approximately follows the Bloch law [23]:

$$M_s(T) = M_s(0)(1 - (T/T_c)^{3/2}). \tag{8}$$

Above, $M_s(0)$ is the magnetization at zero Kelvin, T is the temperature in Kelvin and T_c is the Curie temperature. When the temperature increases, the magnetization of the material decreases, corresponding to the excitation of thermal magnons as discussed in section 2.1. As the Curie temperature T_c is decreased, a greater demagnetization should be achieved for the same change in temperature. Therefore, a higher SW response to the fs-laser is expected for low T_c-materials, such as permalloy doped with a non-magnetic material.

3 Method

The experiments were conducted using a unique setup for BLS measurements and excitation of SWs utilizing a high repetition rate fs-pulsed laser. BLS measurements are done by focusing a laser on the sample as seen in Fig. 7. Some of the photons of the laser will hit the magnons and scatter. This will result in the annihilation or generation of a magnon, in a so-called Anti-Stokes or Stokes process, respectively, and shift the frequency of the scattered photon as described in section 2.5. The frequency change in a scattered photon is dependent on the frequency of the magnon it scatters with and whether a magnon is created or annihilated. The frequency shift can be directly measured using a tandem Fabry-Perot interferometer where each photon is counted, thus a spectrum is constructed which can be subsequently analyzed.

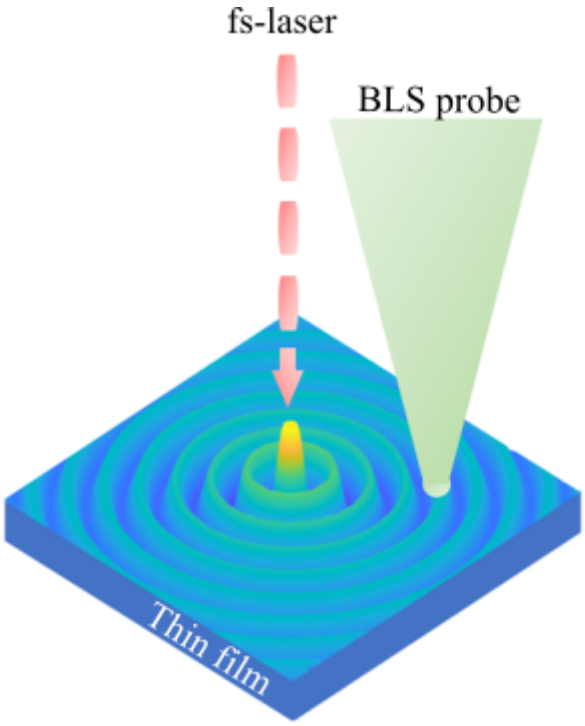

Figure 7: Excitation and detection of spinwaves with light, schematic view of spinwaves being excited by the fs-laser and detected with the BLS microscope.

Measurements of spinwave BLS spectra were made as a function of the external applied magnetic field, where the SW spectra were measured at each applied magnetic field value. This type of measurement was done both with and without the fs-laser being fired at the sample. Additional measurements at a fixed external field value were made where the fs-laser power was varied instead. Finally, all of the previously mentioned measurements were done using Py films of different thicknesses and a 100 nm thick gold-doped Py film.

3.1 Brillouin Light Scattering Microscope

In order to detect and excite the SWs, a fs-laser combined with a BLS-microsope was used (see Fig. 8). The combined microscope works as follows: An external magnetic field is applied through an electromagnet to allow for the tuning of the precession of the magnetic moments and thereby SW frequencies. Then an ultrafast fs-laser hits the ferromagnetic sample with laser pulses at a frequency of 1 GHz, producing ultrafast demagnetization as described in section 2.6. The fact that the femtosecond long laser pulses are being sent out at a frequency of 1 GHz is a large part of what makes this setup unique, as it allows for sustained excitation of the SWs. Without a sufficiently high laser repetition rate the SWs would be damped out and impossible to detect using BLS. When the probe laser hits the sample, at a point of interest, photons are scattered due to the BLS effect. A schematic view of the setup is shown in Fig. 8.

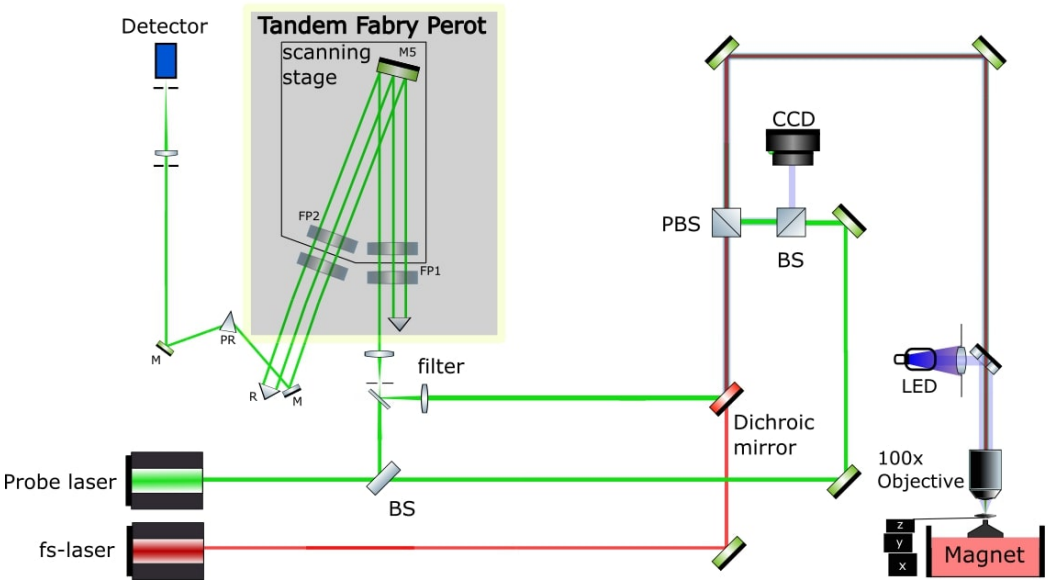

Figure 8: Frequency comb enhanced Brillouin microscopy, a schematic view of the microscope optical layout. The unique setup is nicknamed Frigg Microscope and located at the University of Gothenburg. The pump fs-laser has a wavelength of 816 nm and a pulse width of 120 fs and a repetition rate of 1 GHz. The probe laser is single-mode with a wavelength of 532 nm. The grey box in the top left illustrates the high-resolution 6 pass tandem Fabry-Pérot interferometer. Abbreviations: BS, beam splitter. M, mirror. FP1 & FP2, Fabry-Perot optical cavities (etalons). PR, prism. PBS, polarization beam splitter. R, reflector. CCD, charge couple device camera.

The incident probe light is both monochromatic and linearly polarized. The light inelastically scattered from a magnon experience a change in polarization, as explained in section 2.5. Thus a polarizing beam splitter is used to filter out the elastically re-

flected light and inelastically scattered light from acoustic phonons. The light is then directed to a high-resolution Fabry-Pérot interferometer that can resolve the frequency of the photons, and thus the frequency shift due to the scattering by the SWs.

The BLS microscope has to have a high resolution in MHz (much less than the picometer wavelength change due to the scattering) and a high contrast better than 10^9 – 10^{10} to resolve the SWs. Such requirements require a very special optical solution and therefore a commercial six pass high-resolution tandem Fabry-Pérot Interferometer produced by JRS Scientific Instruments was used in this study. The interferometer consists of Fabry-Pérot etalons which are optical cavities, each made from two parallel reflecting surfaces. The light that enters the etalon will be reflected back and forth between the surfaces, and only photons whose wavelength corresponds to the distance between the two surfaces will resonate with the cavity and be able to pass. The etalons can, therefore, be aligned in such a way that only light with the desired frequency reaches the photo-detector, where the measurements are made. Inside the Fabry-Pérot interferometer used in this experiment, light passes through the etalons six times (see Fig. 8), resulting in the required high contrast measurement of the optical frequency [24]. Synchronization of the etalons spacing with the detector channels allows for assignment of the number of photons detected at each frequency, thus providing a spectrum in frequency space. The use of a BLS-microscope also permits a spatial resolution down to around 320 nm.

3.2 Permalloy Thin Film Deposition

The permalloy (Py) NiFe (80 % nickel and 20 % iron) thin films were fabricated using magnetron sputtering on c-plane (2 cm by 2 cm) sapphire substrates with 0.5 mm thickness. Sputtering is a process in which a solid material is bombarded by energetic atoms or ions in a plasma, which causes microscopic particles, atoms and molecules, to be emitted from the surface of the material and deposited on to the substrate. Sputtering is a useful method for creating thin films with thicknesses in the order nanometres. The film thickness was varied between different samples 20 - 100 nm by controlling the deposition time already calibrated for Py. A thin 10 nm layer of silicon oxides (SiO) was deposited on top of the Py to prevent oxidation. A schematic view of the thin films is found in Fig. 9. The sapphire substrate is much thicker than the films and have an excellent heat conductivity that contributes substantially to heat dissipation. Additional older Py films, that already existed in the lab, doped with small amounts of approximately 10-15% of gold were also used.

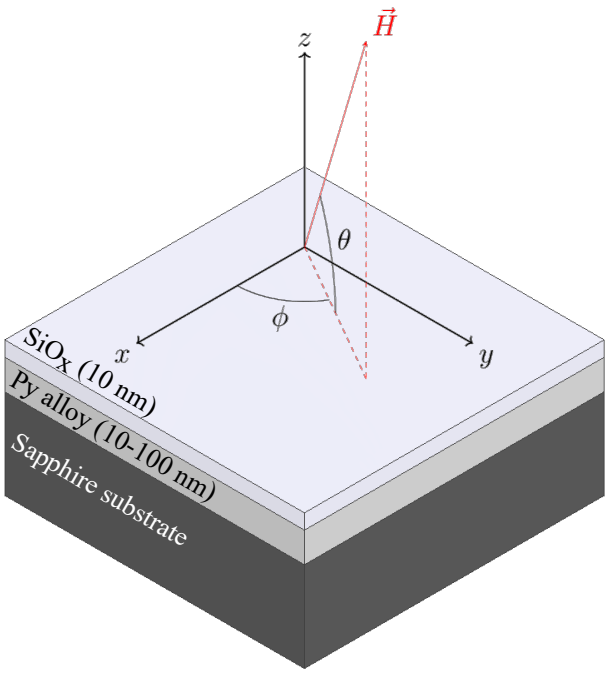

Figure 9: The sample and coordinate system, a schematic view of the thin film samples fabricated using sputtering deposition of permalloy films with thicknesses ranging from 20-100 nm on sapphire substrate with a silicon oxide capping layer. The magnetic field $\vec{H}$ is applied in an oblique direction.

3.3 Experiment Control and Automation

The experimental setup consists of several complex instruments with many different parameters that need to be adjusted or varied. The setup uses a THATec interface for the LabVIEW platform to conduct the experiments, which allowed for centralized control of the instruments and automation of the process with simultaneous multiple parameter control [25]. The measurement data was finally extracted to text files consisting of the used parameters as well as a file for the intensity (BLS-counts) matrix. Additionally, we added a module to control the output polarization analyzer to the setup automation, see Fig. 19 in appendix A.

3.4 Data Analysis

The data was analyzed using a MATLAB-script GUI shown in Fig. 10. The script read the measurement parameters from the extracted files mentioned in the previous paragraph, where one of the text files is combined with the BLS-counts matrix, in order to produce figures such as Fig. 11a and 15a. The modes were then selected and the parameters of interest, frequency and peak intensity, within these modes were extracted by fitting Lorentzian peaks to the data. The determined parameters were fitted to the

dispersion relation of Eq. (6) in order to obtain the saturation magnetization, exchange stiffness and the gyromagnetic ratio. For the fs-laser power dependence, the power of the laser and the counts that correspond to a mode were extracted, and fitted to a Bloch law $T^{3/2}$ model [13] with the following form:

$$\delta M_s^2 = A^2(t_r^{3/2} - (t_r + F)^{3/2})^2. \tag{9}$$

Where A and t_r are the fitted parameters, and F is the fluence of the fs-laser. It is assumed that the temperature is proportional to the laser fluence.

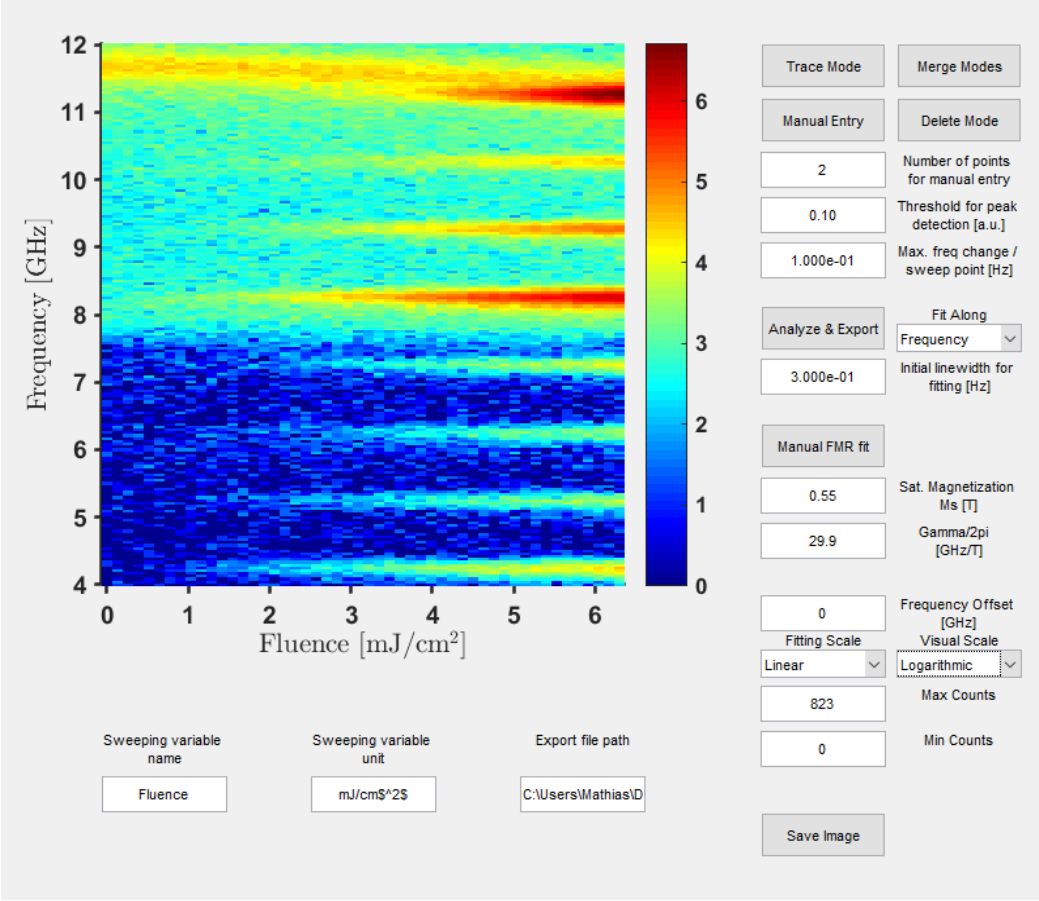

Figure 10: MATLAB program used in the data analysis, The image show a snapshot of the user interface of the MATLAB script used to extract, process and visualize the data. The program was substantially improved during this study.

The MATLAB script used originated as a somewhat bare-bones program capable of extracting data by fitting Lorentzian distributions to the data for every value of the swept parameter, those being fs-laser fluence or external magnetic field strength. The program has been enhanced, by the authors of this study, with many new features and much has been done to improve both its latency and readability. Following is a short

summary of said improvements. To expedite the analysis of large sets of data, a recursive search function that automatically detects and loads measurement data has been programmed. It was found that to properly extract data from some measurements, the Lorentzian fitting could be conducted over the swept parameter instead of the frequency, that is to have the swept parameter as the x-axis variable. This functionality was added. A simple function to plot the FMR mode was also added for a quick inspection. In order to visually compare different measurements with different signal intensities, a logarithmic view feature was implemented. The functionalities to shift the frequencies to align modes and to select the minimum and maximum values of the color scale were also added. With several features required to produce visually pleasing images all ready implemented, a dedicated function, the ”Save Image” button, to export figures was created.

4 Results and Discussion

In this section, the results will be presented and discussed. It was found that the SWs in thinner magnetic films were more excited by the fs-laser, leading to greater SW intensity. The SW intensity was found to approximately decrease exponentially with increasing film thickness. It was also observed that the fs-laser was able to excite SW modes up to 15 GHz, i.e. 15 times the fs-laser repetition rate. The gold-doped Py sample had roughly an order of magnitude greater intensity compared to a pristine Py sample of equal thickness. Due to the Covid-19 outbreak and one of the controller computers of the setup, a number of follow up measurements that had been intended could not be carried out. This has limited the scope of the comparisons between the doped and pristine Py samples, as only the 100 nm doped sample was thoroughly studied. However, preliminary results on doped samples of different thicknesses indicated similar behavior to the pristine case with respect to the excited SWs and the power dependence trends.

The results section will be arranged as follows, first we discuss the general behaviour of the SWs in a 100 nm thick Py film, with and without fs-laser. Then we examine the laser power influence on the sustained SWs, subsequently we compare the behaviour of the sustained SWs in different thicknesses of the Py films. Finally we show the effect of doping Py and the implications that it has on the sustained SW intensity.

4.1 Magnetic Field Sweeps

First we examine the SW frequency field dependence. As discussed in sections 2.2 - 2.4, such measurements can be used to extract the magnetic saturation M_s, the gyromagnetic ratio γ, and the exchange stiffness A_{ex} from the dispersion relation in Eq. (6). The way this is done is illustrated in Fig. 11, for a 100 nm permalloy film. The color plots show the logarithm of the BLS counts spectra which is proportional to the number of detected magnons (via detected photons using BLS) as a function of the external magnetic field.

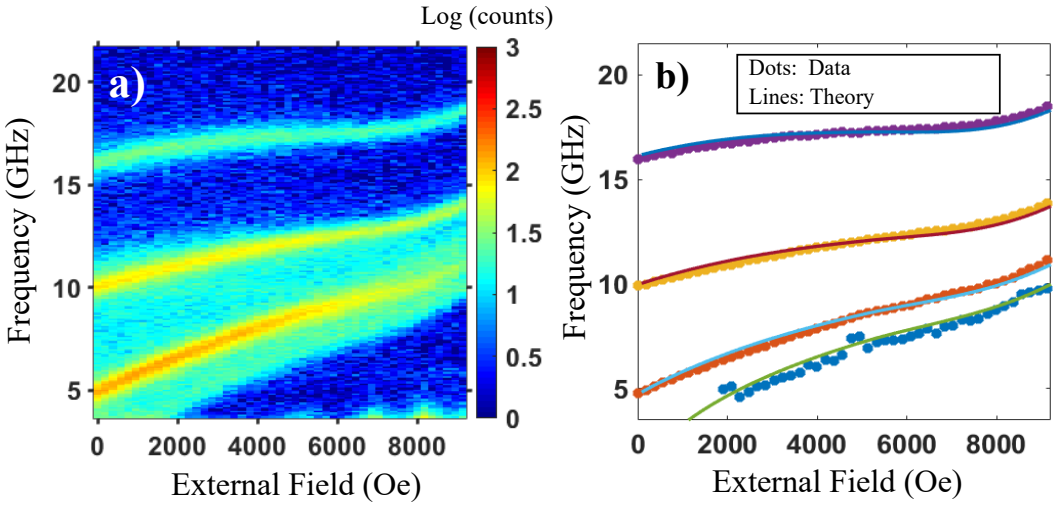

Figure 11: Spinwave frequency as function of applied magnetic field, (a) μ-BLS (logarithmic scale) spectrum as a function of the applied magnetic field for the 100 nm permalloy film. The local intensity maxima correspond to the spinwave modes. (b) The data points are extracted SW frequencies at each field value in (a), the lines are fits to the theoretical SW dispersion relation, Eq. (6), which is used to extract the material magnetic parameters M_s, γ, and A_{ex}.

In Fig. 11(a) several SW modes can be examined. From lowest to the highest frequency, they are the FMR, and then the first, second, and third PSSWs. The width of the FMR region is due to the dispersion relation, as the microscope lacks k-vector resolution it detects all of the in-plane SWs up to the resolution of the microscope. The field and frequency for the maxima corresponding to the SW modes are extracted by a multipeak fitting of the spectrum with each peak corresponding to a single symmetric Lorentzian. Afterward, the dispersion relation is fitted to these points as seen in Fig. 11(b). This allows for the extraction of the magnetic material parameters M_s, γ, and A_{ex}. For this 100 nm film $M_s = 0.82$ T, $\gamma = 29.4$ GHz$/(2\pi \cdot \mathrm{T})$ and $A_{ex} = 10.1$ pJ/cm, which are in good agreement with typical Py parameters [26].

4.2 Magnetic Field Sweeps with Femtosecond Laser

To understand the effect of the fs-laser on the frequency spectrum of the SWs, similar measurements to those in the previous section must be made with the fs-laser turned on. From these measurements, both qualitative and quantitative comparisons can be made to the thermal SWs. In this section, we will restrict the study to the qualitative difference for a selected fs-laser fluence.

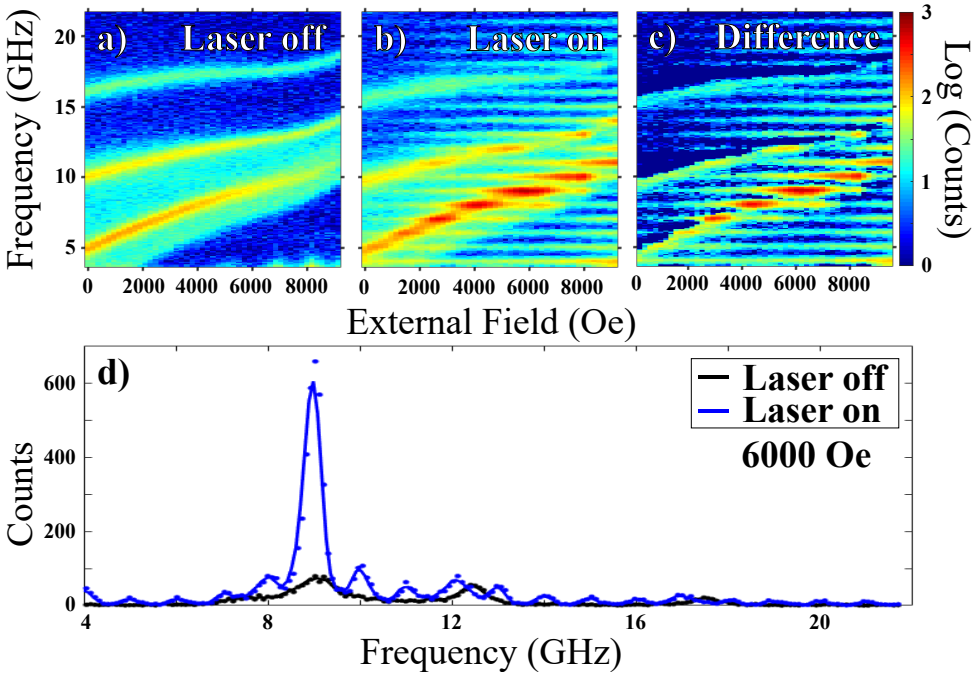

Figure 12: Effect of fs-laser on spinwaves spectra, (a) μ-BLS (logarithmic scale) spectrum as a function of the applied magnetic field (b) μFC-BLS spectrum where the fs-laser is turned on with a fluence of 5.04 mJ/cm^2. (c): The difference between (a) and (b) where negative values set to zero. (d) μ-BLS (linear scale) spectra at 6000 Oe with both laser on and off.

Figure 12 compares the external magnetic field sweeps with and without the fs-laser for the 100 nm Py film. The laser induced SWs in Fig. 12(b) exhibit similar field dependence as the thermally generated SWs in Fig. 12(a). However, unlike the thermally excited SWs, the laser induced SWs are clearly excited at frequencies that are multiples of the fs-laser repetition rate of 1 GHz, as can be seen in Fig. 12(d). This happens as the spinwaves which are in phase with the repetition rate gets amplified.

The amplification is higher for the PSSWs than the FMR and other SWs. This is likely due to that the PSSWs are excited along the thickness of the film, where the region is mostly stimulated by the fs-laser. The in-plane wavevector SWs and to lesser degree the FMR propagates and extend along the plane of the film and are coupled to the unstimulated regions of the film, resulting in a higher damping.

Moreover, the fs-laser induced SWs seemingly only amplifies the thermal SWs up to a frequency of about 15 GHz, as the upper most PSSWs seems to be unaffected by the fs-laser. This restriction is due to the SW damping and the amplitude of demagnetization. This means that the SWs above 15 GHz are completely dampend between two pulses of the fs-laser. The implications of this is important considering that the sought after SW applications are in the high frequency regime from GHz to

THz. Further studies into what determines this limit are of high interest, whether it is the damping of the mode or additionally the overlap with the fs-laser spot, tuning the laser repetition rate to a few tens of GHz would be probably capable of exciting SWs up to hundreds of GHz.

Figure 12(c) shows the differences between Fig. 12(a) and (b). This figure is presented with negative count values set to zero in a logarithmic scale, this is done to make the changes clearer. It is clear that the frequencies of the different modes, have decreased. This decrease in frequency should be caused by the increase in the local equilibrium temperature as the fs-laser heats the sample, causing ΔM to increase as described in Fig. 6. This decrease in magnetization lowers the frequency of the different modes as described in Eq. (4) and (6). It can be noted that the decrease is larger for higher modes. This is described by theory as M_s is multiplied with the k-vector squared, thus modes with a larger k-vector are more sensitive to changes in M_s.

4.3 Femtosecond Laser Power Dependece of Spinwaves

After examining the effects of the fs-laser on the spinwave dispersion, the laser power dependence of the excited SWs was studied, as seen in Fig. 13. Furthermore, the BLS counts for the different modes were extracted. These are of interest as the relationship between the local temperature and the amount of generated magnons is given by the Bloch $T^{3/2}$ law (Eq. (9)). To check if this holds true the extracted BLS counts for the different modes and the 1 GHz harmonics were fitted to Eq. (9) with the assumption that the local temperature is proportional to the applied laser power.

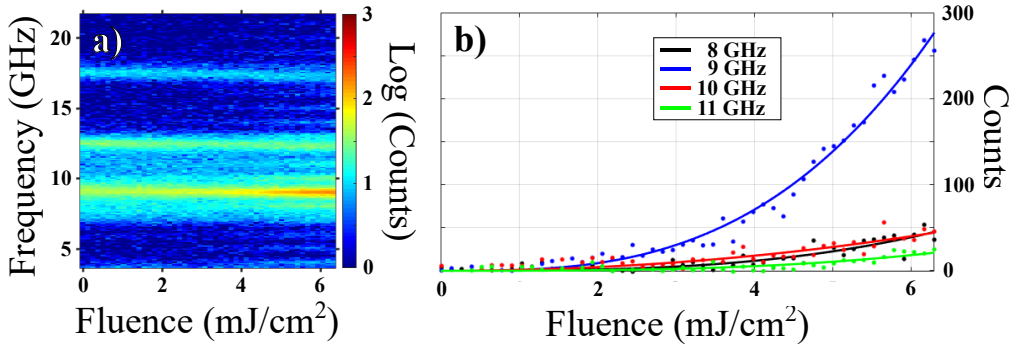

Figure 13: fs-laser power sweep, (a) SW intensity as a function of laser fluence. (b) Points are SW intensity for frequencies of 8, 9, 10 and 11 GHz, as function of the laser fluence extracted from (a). The solid lines are fits of the BLS spectra to Bloch $T^{3/2}$ law, Eq. (9).

The SW intensity as a function of the applied laser power (laser fluence) and frequency for an undoped 100 nm thin film is shown in Fig. 13(a). The SW intensity is also

shown as a function of only fluence for the different frequency modes in Fig. 13(b). It can be seen in Fig. 13(b) that the Bloch law fits the experimental data for 100 nm thin film reasonably well.

4.4 Sustained Spinwaves vs. Film Thickness

In order to characterize the efficiency and the behavior of fs-laser sustained SWs with respect to the film thicknesses, both field and fs-laser power sweep measurements were conducted using a series of films with different thickness (20 to 100 nm). Figure 14 shows field sweeps, like those in Fig. 11 and 12, for permalloy films with thicknesses of 20 and 60 nm.

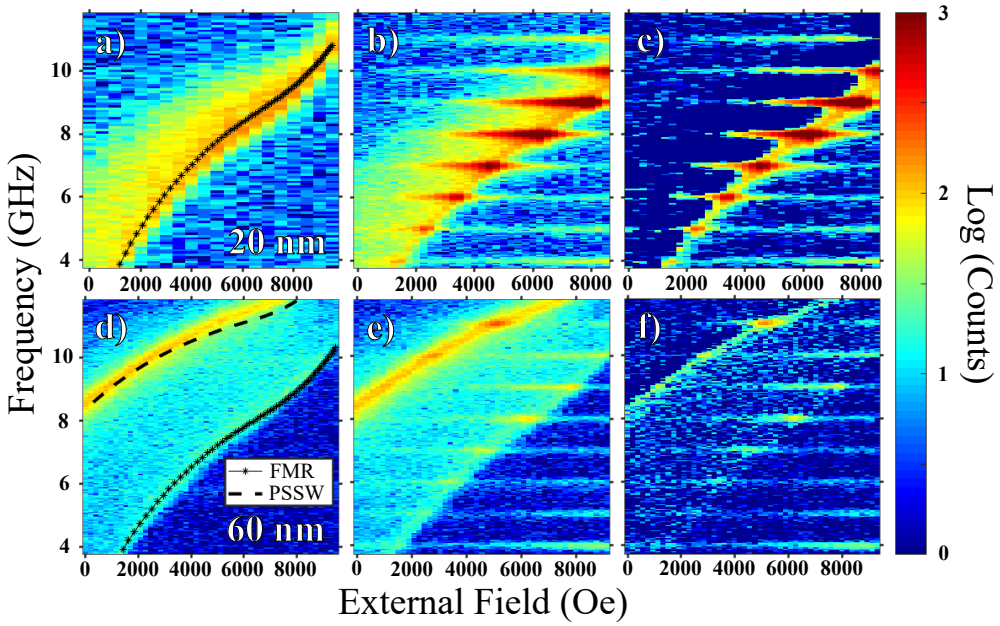

Figure 14: fs-laser sustained SWs in permalloy films with different thicknesses, (a)-(f) BLS spectra of SWs versus magnetic field. (a), (d) BLS spectra as a function of the magnetic field, the overlaid lines are the theoretical dispersion relation for different SW modes for 20 and 60 nm, respectively. (b), (e) BLS spectra vs. magnetic field strength with the fs-laser on with a laser fluence of 2.52 mJ/cm^2 for 20 nm and 60 nm respectively. (c), (f) The difference between the field sweeps with and without the fs-laser on for 20 and 60 nm, respectively.

From Fig. 14(a) and (d), it is clear that as the thickness of the film increases more SW modes become visible, as their frequency reduces due to the wavelength increase, via the effect described in section 2.3. These modes are the PSSWs as shown in section 4.1. The values of the magnetic saturation M_s and the exchange stiffness A_{ex} can be determined using the Kittel equation, Eq. (4), and the dispersion relation, Eq. (6). This is done for the field sweeps without fs-laser and the values of M_s and A_{ex} are shown in

Table 1. The table shows that the exchange stiffness is lower for 100 nm compared to 60 nm. The 20 nm sample has no PSSWs hence it is not possible to extract a value for A_{ex} at 20 nm thickness. But nevertheless all values are comparable and the fabricated films could be used to verify the thickness dependence of the fs-laser SW excitation.

Table 1: The table shows the measured values for each thickness of the undoped permalloy films. M_s and $\gamma/2\pi$ are fairly constant.

Thickness (nm)	M_s (T)	$\gamma/2\pi$ (GHz/T)	A_{ex} (pJ/cm)
20	0.85 ±0.01	31.0 ±0.1	(No PSSWs)
60	0.82 ±0.01	29.4 ±0.1	10.6 ±0.05
100	0.82 ±0.01	29.4 ±0.1	10.1 ±0.04

Furthermore, when comparing the field sweeps with and without the fs-laser, one can note that the 60 nm sample is less stimulated by the fs-laser as compared to the 20 nm sample for the same fluence. This suggests that the demagnetization amplitude has increased more for the thinner sample. Additionally, the colormap difference in Fig. 14(c) and (f), shows that the incoherent magnon spectra has shifted to lower frequencies, especially for the 20 nm thick sample, presented in Fig. 14(c). This denotes a reduction of the equilibrium magnetization parameters, which indicates a higher residual temperature in the films. These observations, the change in ultrafast demagnetization amplitude and residual temperature, operate on vastly different timescales, however we speculate that they both are caused by a decrease in local energy in thicker samples. We will discuss this more thoroughly when comparing the fs-laser power sweeps for different sample thicknesses.

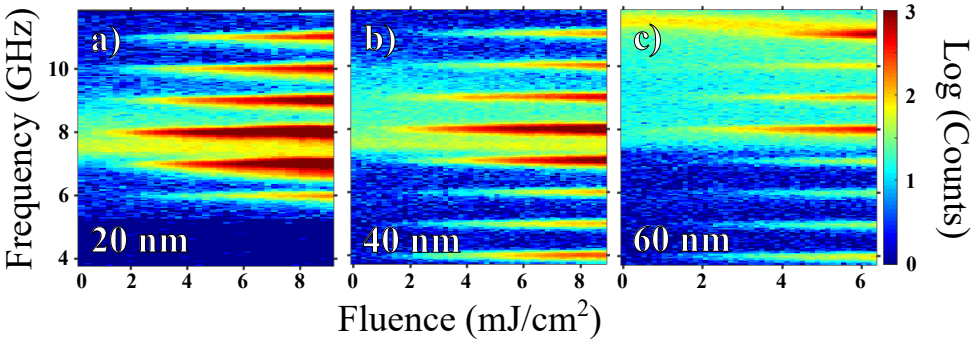

Figure 15: Sustained SWs in permalloy films with different thicknesses as a function of laser power, (a)-(c) BLS spectra of SWs as a function of fs-laser fluence with a fixed external field of 6000 Oe, for 20, 40 and 60 nm, respectively.

The fs-laser power sweeps for the different thicknesses show that the laser has a greater effect on the thinner samples, which is illustrated in Fig. 15. As the thickness decreased

the intensity of all the harmonics increased. An additional observation is the substantial increase of the PSSWs compared to the other SWs with in-plane wavevectors.

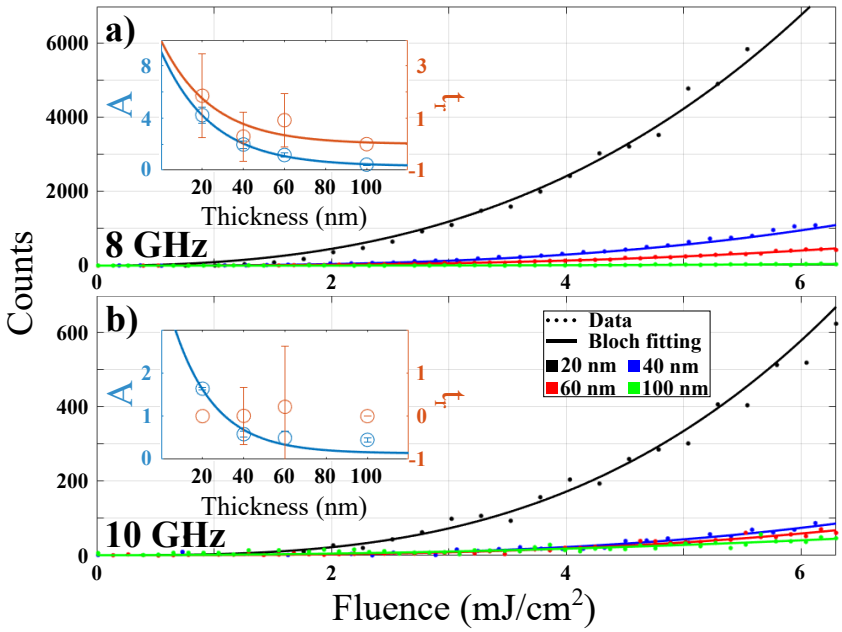

Figure 16: Sustained SW efficiency for different thicknesses, the figure shows the sustained SWs at 8 and 10 GHz modes for samples with different thicknesses. Lines are theoretical fits to the Bloch equation, Eq. (9). The insets show the extracted parameters from the theoretical fit as a function of the film thickness for 8 and 10 GHz, respectively. When appropriate, exponential functions have been fitted to the parameters.

The Bloch law (Eq. (8)) seems to describe the SW behavior quite well. In Fig. 16 the magnon count is shown as a function of laser fluence for different sample thicknesses and two different frequencies. These modes are chosen as they do not overlap with a PSSW for any of the thicknesses, making them more readily comparable. The curves follow the observed general trend with thicker samples having lower magnon counts. The insets show parameters A and t_r from Eq. (9) as a function of sample thickness for the two frequencies. The parameter A reflects the intensity of the mode, as can be seen in the equation. The solid blue trend line, a decaying exponential, shows that the intensity decreases with increasing sample thickness.

The second parameter from Eq. (9), t_r, is less intuitive in its function. It reflects where along the fluence axis the mode starts to rise, a low value signifies that the mode slowly rises whilst a high value means that it rises quickly. In the insets, we see that t_r seems to approach zero with increasing sample thickness at 8 Ghz. The trend is not as obvious, however, for the 10 GHz case, it seems to be constantly zero. This can be interpreted as the thinner samples being more readily excited by the laser, compared

to the thicker samples, which need a much higher fluence to show the same intensity. One can also note the much greater uncertainty in this parameter, this is because it has less of an effect on the curve as compared to A.

As seen in Fig. 16, the thickness of the film has a large effect on the optically excited SW intensity. Our interpretation of this is that there is a reduction in ultrafast heating for thicker samples due to an increased reflectivity of these films. Previous studies have shown that the absorption rate of thin nickel films on sapphire substrates does indeed decrease with the film thickness [27]. This behaviour can be seen for many other metals, such as iron, as well [28]. Therefore, we expect permalloy to behave similarly. This lower absorption means that more of the light from the fs-laser is reflected leading to less transient heating in thicker samples.

Additionally, the local energy is reduced due to the ultrafast heat transport of hot electrons. When the fs-laser strikes the sample, it delivers its energy to the electrons as described by the three temperature model. Since the penetration depth of the laser is around 10-20 nm in permalloy [29], these high energy electrons will quickly diffuse out into the less affected regions of the sample. This diffusion happens on a timescale that is relevant to the ultrafast demagnetization [30, 31]. Moreover, the decrease in local transient heat, on an ultrafast timescale, causes a decrease in the equilibrium temperature bath. This will lead to a lower demagnetization amplitude for thicker samples.

With the strong thickness dependence seen, we conclude that in future magnon applications using optics to excite SWs, the thickness of the SW device, in conjunction with the laser fluence, will be an important design criterion.

4.5 Effect of Doping

In the previous section, we showed systematically that sustainable SWs could be excited in thin Py films, with the efficiency being higher for thinner films. A question that arises is how to further enhance the efficiency of the excitation. A straight forward answer would be to use materials with lower damping or otherwise to enhance the demagnetization amplitude further. In this study, we took the opportunity of testing similar samples which existed in the lab. A set of Py samples which had been deposited earlier for the sake of the project, were initially characterized during the project and discarded due to a contamination of what we expect to be gold from the target housing and enclosure during the deposition.[1] The samples consist of a 100 nm film, that shows lower M_s and A_{ex} than the pure film and it is expected to have lower Curie temperature as well [32].

[1]The sample doping ratio verification couldn't be characterized yet due to the concurrent covid-19 situation.

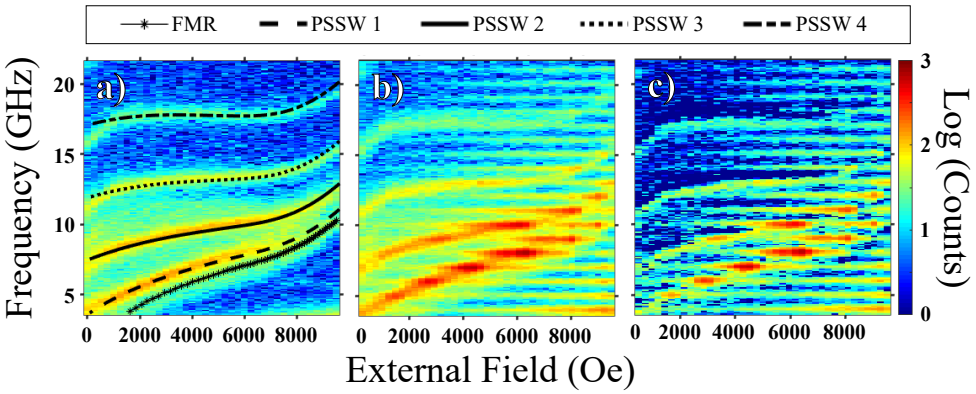

Figure 17: SW BLS spectrum field dependence, with and without fs-laser, for the doped permalloy sample. (a),(c) The SW BLS spectra as a function of applied field where (a) shows the SWs at thermal equilibrium, and the overlaid lines are theoretical fits. (b) shows the SW spectra with the fs-laser applied at a 2.52 mJ/cm^2 fluence. (c) shows the difference between (a) and (b), where negative values are set to zero.

Figure 17(a) shows that the PSSWs have decreased in frequency, making more of them visible in the measured frequency span. This decrease in frequency can be understood by considering the dispersion relations described in section 2.3. The doping, which probably is gold, is of a non-magnetic material, thus, as it is added to permalloy the total magnetization is expected to decreases, as can be observed in Fig. 6. Therefore, due to the role of M_s in the dispersion relations, as it decreases it leads to a lower frequency for all modes. The extracted values from the fitting to the dispersion relations are as follows: $M_s = 0.74 \pm 0.02$ (T), $\gamma/2\pi = 28.0 \pm 0.1$ (GHz/T) and $A_{ex} = 6.4 \pm 0.03$ (pJ/cm).

The PSSWs in Fig. 17(a) deviate slightly from their theoretical values at low and high magnetic field strengths. The reason for the poor fitting at the low field compared to the pure film, is likely due to small magnetic anisotropy neglected in our calculations. Meanwhile, the high field deviation is most likely poorly fit due to a small difference between the computed and the applied magnetic field from the electromagnet in our experimental setup. As for the extracted values, in comparison with earlier experimental data for gold doped films [26], it seems like our 100 nm sample is doped with approximately 11 - 14% Au.

Figure 17(b) shows similar features compared to the undoped case. The fs-laser is able to stimulate the modes up to 15 GHz. Finally, in Fig. 17(c) we once again see the effect of heating the sample as the modes decrease in frequency. Qualitatively, little difference is to be found compared to the undoped case, as the frequency decrease seem to be of the same magnitude between the corresponding modes of the two samples.

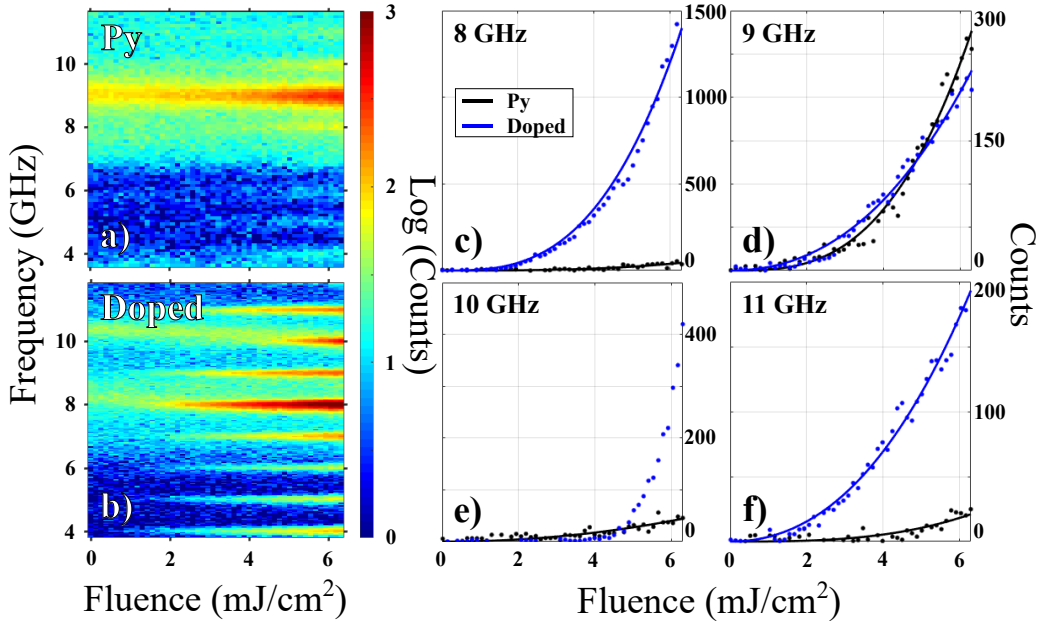

Figure 18: Sustained SW efficiency comparison for pure and doped permalloy, a comparison between the Py and doped 100 nm sample fs-laser power dependence. Both measurements are conducted with a constant external field strength of 6000 Oe.

Table 2: Extracted parameters from power sweeps ($L = 100$ nm), corresponding parameters to the fitted curves in Fig. 18.

	8 GHz	9 GHz	10 GHz	11 GHz
A Py	0.424 ± 0.046	1.051 ± 0.175	0.091 ± 1.112	0.289 ± 0.039
A Doped	2.365 ± 0.058	0.568 ± 0.253	(No Fit)	0.521 ± 0.220
t_r Py	0	$46.71 \times 10^{-9} \pm 0.598$	55.96 ± 142.2	0
t_r Doped	0	5.000 ± 6.694	(No Fit)	4.998 ± 6.356

In Fig. 18 we see the stark contrast between the doped and undoped permalloy. Firstly, note the big difference between the two color plots. In the undoped case, most modes are too weak to extract any data, and several of the modes are barely visible. Also, note that in the undoped case only one PSSW is visible at 9 GHz, while in the doped case two PSSWs can be seen, one just above 8 GHz and one just above 10 GHz. For the 8 GHz mode, we see that the doped sample is two orders of magnitude more intense. This great difference is likely due to the fact that the doped 8 GHz mode overlaps with a PSSW in contrast to the undoped mode. The 9 GHz modes, however, are of the same magnitude, and in this case, the situation has been flipped with the undoped mode overlapping with a PSSW whilst the doped one does not.

For the 10 GHz modes, something interesting happens. As noted earlier, we see a PSSW a bit above 10 GHz in the doped color plot, as the fluence increases this PSSW

decreases in frequency and it eventually begins to overlap with the 10 GHz mode at around 4 mJ/cm^2. Unlike the other PSSWs this overlapping effect is not consistent for the entire fluency span. This gives rise to an extremely rapid increase in intensity with increasing fluence as not only is the sample heated, giving rise to more magnons, but the overlap of the mode with a PSSW increases at the same time. This is reflected in the figure as the doped 10 GHz mode does not fit well to the Bloch $T^{3/2}$ law (Eq. (8)), thus it has been left unfitted in the plot. Unexpectedly, the intensity of the doped mode is only around one order of magnitude stronger compared to the undoped mode.

Comparing the two 11 GHz modes, we see that the doped mode is one order of magnitude brighter. These modes are perhaps the best in regards to comparing the samples as both modes are within the FMR region whilst not overlapping with a PSSW, thus they should be very comparable. Still, we note one order of magnitude difference in intensity. In general, it seems that the doped sample modes are one order of magnitude brighter, but whenever a PSSW overlaps with a mode, that mode has its intensity increased by one order of magnitude. This holds true for all the studied modes except the 10 GHz modes, however, as discussed that mode is a special case.

5 Conclusions and Outlook

The fs-laser was found to generate sustained SW with high intensity at multiples of the used 1 GHz fs-laser repetition rate for waves up to a frequency of about 15 GHz. The spinwave BLS counts also indicated a stronger than parabolic relation to the fs-laser fluence. Furthermore, the results clearly show that laser excitation of sustained SWs is possible for all the measured thicknesses between 20 and 100 nm, and the efficiency is inversely related to the thickness. Finally, the measurements suggested the same behaviour but an enhanced efficiency in the gold doped samples. The greater efficiency is caused by the larger demagnetization in the low-T_c material. The impact of the laser-induced heating on $M(T)$ increases as the temperature approaches T_c, as discussed in section 2.6.

An interesting object of further studies would be to examine how the laser repetition rate affects the range of excitation. For example, if a laser with a repetition rate of 15 GHz is used, would it be possible to excite the spinwaves in the 15-225 GHz region? Alternatives to permalloy could also be examined, to determine how different SW damping could alter the frequency region.

It would also be interesting to examine the frequency shift due to the change in equilibrium temperature. A potential relation between the local temperature and the fs-laser induced demagnetization can be constructed using the BLS-microscope and an additional temperature controlled SW measuring technique, e.g. a FMR-spectroscope. The FMR-spectroscope would be used to map the relation between the magnetic parame-

ters A_{ex} and M_s, and the temperature in the sample. This could be compared to the SW parameters extracted from the BLS-microscope measurements made in this thesis to determine a local temperature.

References

[1] Bloch F. Zur Theorie des Ferromagnetismus. Zeitschrift für Physik. 1930;61:206–219.

[2] Hofstadter R. Felix Bloch. The National Academies Press; 1994. Available from: https://www.nap.edu/read/4547/chapter/3.

[3] Kruglyak VV, Demokritov SO, Grundler D. Magnonics. J Phys D [Internet]. 2010 jul;43(26):264001. Available from: http://stacks.iop.org/0022-3727/43/i=26/a=264001?key=crossref.7d59bbfceddaf0f03df576a620cfcdf3.

[4] Lenk B, Ulrichs H, Garbs F, Münzenberg M. The building blocks of magnonics. Physics Reports [Internet]. 2011 January;507(4):107–136.

[5] Chumak AV, Vasyuchka VI, Serga AA, Hillebrands B. Magnon spintronics. Nat Phys [Internet]. 2015 jun;11(6):453–461. Available from: http://www.nature.com/articles/nphys3347.

[6] Kittel C. Introduction to Solid State Physics. 8th ed. Wiley; 2004.

[7] Sebastian T, Schultheiss K, Obry B, Hillebrands B, Schultheiss H. Micro-focused Brillouin light scattering: imaging spin waves at the nanoscale. Frontiers in Physics [Internet]. 2015;3:35. Available from: https://doi.org/10.3389/fphy.2015.00035.

[8] Wolf P. Free Oscillations of the Magnetization in Permalloy Films. J Appl Phys [Internet]. 1961 mar;32(3):S95–S96. Available from: http://aip.scitation.org/doi/10.1063/1.2000514.

[9] McDonald L. Magnonics, an alternative to conventional electronics [Internet]; 2019. Available from: https://ceramics.org/ceramic-tech-today/basic-science/magnonics-an-alternative-to-conventional-electronics.

[10] Demokritov SO, Slavin AN. Magnonics: From fundamentals to applications. Topics in Applied Physics. Springer Nature; 2013.

[11] Torrejon J, Riou M, Araujo FA, Tsunegi S, Khalsa G, Querlioz D, et al. Neuromorphic computing with nanoscale spintronic oscillators. Nature [Internet]. 2017 Jul;547(7664):428–431. Available from: http://arxiv.org/abs/1701.07715http://www.nature.com/doifinder/10.1038/nature23011.

[12] Zahedinejad M, Awad AA, Muralidhar S, Khymyn R, Fulara H, Mazraati H, et al. Two-dimensional mutually synchronized spin Hall nano-oscillator

arrays for neuromorphic computing. Nature Nanotechnology [Internet]. 2020 December;15:47–52. Available from: http://dx.doi.org/10.1038/s41565-019-0593-9.

[13] Awad AA, Muralidhar S, Alemán A, Khymyn R, Dvornik M, Hanstorp D, et al.. Sustained coherent spin wave emission using frequency combs; 2019. Available from: https://arxiv.org/pdf/1908.03388.pdf.

[14] Chen T, Dumas RK, Eklund A, Muduli PK, Houshang A, Awad AA, et al. Spin-Torque and Spin-Hall Nano-Oscillators. Proc IEEE [Internet]. 2016 Oct;104(10):1919–1945. Available from: https://www.diva-portal.org/smash/get/diva2:868735/FULLTEXT01.pdf.

[15] van Kampen M, Jozsa C, Kohlhepp JT, LeClair P, Lagae L, de Jonge WJM, et al. All-optical probe of coherent spin waves. Phys Rev Lett [Internet]. 2002;88(22):227201. Available from: https://www.researchgate.net/publication/11315703_All-Optical_Probe_of_Coherent_Spin_Waves.

[16] Jäckl M, Belotelov VI, Akimov IA, Savochkin IV, Yakovlev DR, Zvezdin AK, et al. Magnon Accumulation by Clocked Laser Excitation as Source of Long-Range Spin Waves in Transparent Magnetic Films. Phys Rev X [Internet]. 2017 apr;7(2):021009. Available from: http://link.aps.org/doi/10.1103/PhysRevX.7.021009.

[17] Savochkin IV, Jäckl M, Belotelov VI, Akimov IA, Kozhaev MA, Sylgacheva DA, et al. Generation of spin waves by a train of fs-laser pulses: a novel approach for tuning magnon wavelength. Sci Rep [Internet]. 2017 dec;7(1):5668. Available from: http://www.nature.com/articles/s41598-017-05742-x.

[18] Gurevich A, Melko G. Magnetization oscillation and waves. 1st ed. CRC Press, Inc.; 1996.

[19] Kalinikos B, Slavin A. Theory of dipole-exchange spin wave spectrum for ferromagnetic films with mixed exchange boundary conditions. Journal of Physics C: Solid State Physics [Internet]. 1986;19(35):7013. Available from: https://iopscience.iop.org/article/10.1088/0022-3719/19/35/014/pdf.

[20] Beaurepaire E, Merle JC, Daunois A, Bigot JY. Ultrafast Spin Dynamics in Ferromagnetic Nickel. Phys Rev Lett [Internet]. 1996 May;76:4250–4253. Available from: https://link.aps.org/doi/10.1103/PhysRevLett.76.4250.

[21] Koopmans B, Malinowski G, Dalla Longa F, Steiauf D, Fähnle M, Roth T, et al. Explaining the paradoxical diversity of ultrafast laser-induced demagnetization. Nat Mat [Internet]. 2010;9(3):259–265. Available from: https://doi.org/10.1038/nmat2593.

[22] Kirilyuk A, Kimel AV, Rasing T. Ultrafast optical manipulation of magnetic order. Rev Mod Phys [Internet]. 2010 Sep;82:2731–2784. Available from: https://link.aps.org/doi/10.1103/RevModPhys.82.2731.

[23] Ashcroft N, Mermin D. Solid State Physics. 1st ed. Harcourt College Publishing; 1976.

[24] Schuleitss H, Hillebrands B. TFPDAS4 User's Manual; 2012.

[25] THATec Innovation;. Available from: https://www.thatec-innovation.com/.

[26] Yin Y, Pan F, Ahlberg M, Ranjbar M, Dürrenfeld P, Houshang A, et al. Tunable permalloy-based films for magnonic devices. Phys Rev B [Internet]. 2015 Jul;92:024427. Available from: https://link.aps.org/doi/10.1103/PhysRevB.92.024427.

[27] Schellekens AJ, Verhoeven W, Vader TN, Koopmans B. Investigating the contribution of superdiffusive transport to ultrafast demagnetization of ferromagnetic thin films. Applied Physics Letters [Internet]. 2013;102(25):252408. Available from: https://doi.org/10.1063/1.4812658.

[28] Krayer LJ, Kim J, Munday JN. Near-perfect absorption throughout the visible using ultra-thin metal films on index-near-zero substrates. Opt Mater Express [Internet]. 2019 Jan;9(1):330–338. Available from: http://www.osapublishing.org/ome/abstract.cfm?URI=ome-9-1-330.

[29] Tikuišis KK, Beran L, Cejpek P, Uhlířová K, Hamrle J, Vaňatka M, et al. OPTICAL AND MAGNETO-OPTICAL PROPERTIES OF PERMALLOY THIN FILMS IN 0.7–6.4eV PHOTON ENERGY RANGE. Materials Design [Internet]. 2017;114:31 – 39. Available from: http://www.sciencedirect.com/science/article/pii/S0264127516313351.

[30] Salvatella G, Gort R, Buhlmann K, Däster S, Vaterlaus A, Acremann Y. Ultrafast demagnetization by hot electrons: Diffusion or super-diffusion? Structural Dynamics [Internet]. 2016 09;3:055101. Available from: https://journals.aps.org/prl/abstract/10.1103/PhysRevLett.105.027203.

[31] Battiato M, Carva K, Oppeneer PM. Superdiffusive Spin Transport as a Mechanism of Ultrafast Demagnetization. Phys Rev Lett [Internet]. 2010 Jul;105:027203. Available from: https://link.aps.org/doi/10.1103/PhysRevLett.105.027203.

[32] Luo C, Fu Y, Zhang D, Yuan S, Zhai Y, Dong S, et al. Temperature dependent coercivity and magnetization of light rare-earth Nd doped permalloy thin films. Journal of Magnetism and Magnetic Materials [Internet]. 2015;374:711 – 715.

Available from: http://www.sciencedirect.com/science/article/pii/S0304885314008336.

A Thatec motor controller

In order to get some insight into how the experimental setup is controlled, a motor controller program was written in labview. The motor rotates a polarizer, allowing for remote control of the polarization of the light entering the interferometer in the setup. This should allow for the study of for example phonons in the material. The program uses the Thorlabs kinesis motor control software.

Front Panel Block Diagram

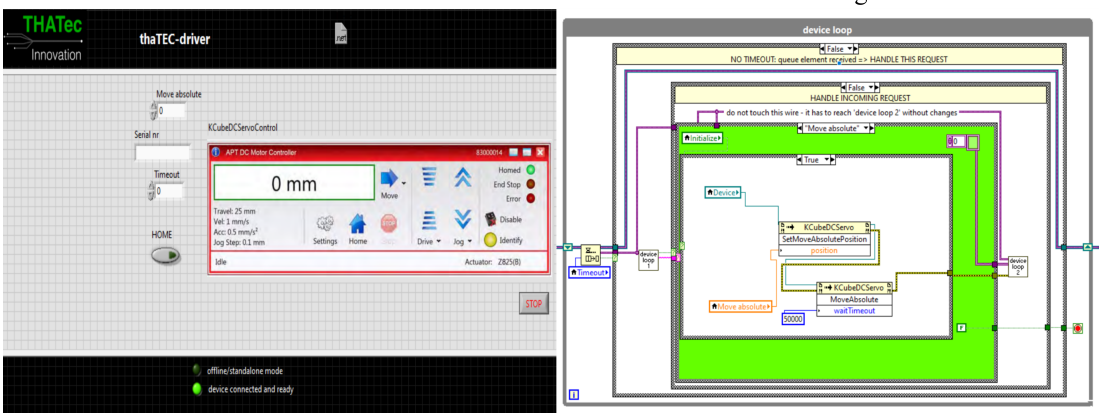

Figure 19: Seen here is the front panel and block diagram of a Thatec-compatible labview program. The program is used to control a T- or K-cube Thorlabs motor remotely.

DEPARTMENT OF PHYSICS
CHALMERS UNIVERISTY OF TECHNOLOGY
UNIVERSITY OF GOTHENBURG
Gothenburg, Sweden 2020

UNIVERSITY OF
GOTHENBURG

CHALMERS
UNIVERSITY OF TECHNOLOGY